

# Application of the CATNLF Design Method to a Transonic Transport Empennage Using CDISC

Brent W. Pomeroy,\* Richard L. Campbell,† Michelle N. Banchy,‡ and Brett R. Hiller‡  
*NASA Langley Research Center, Hampton, VA, 23681*

A novel Crossflow Attenuated Natural Laminar Flow (CATNLF) design method has been developed to achieve laminar flow on aircraft empennage at transonic flight conditions. This approach has been applied to the design of a nonlifting vertical tail using CDISC, a knowledge-based aerodynamic design tool developed at the NASA Langley Research Center. A horizontal tail was also designed using an enhanced CATNLF design approach for low-lift components. CDISC was coupled with USM3D-ME, a Navier-Stokes computational fluid dynamics solver. Stability and transition software was used to determine the laminar extent on the surfaces. Results indicate laminar flow can be sustained at midcruise conditions to about  $x/c=0.40$  on the vertical tail and as much as  $x/c=0.65$  on the horizontal tail lower surface. Transonic longitudinal off-design analysis indicates minimal change in the laminar extent. However, nonzero sideslip angles at transonic conditions can cause premature transition relative to the midcruise condition.

## Nomenclature

$C$	=	surface curvature (nondimensionalized by local chord)
$C_{f,x}$	=	skin friction coefficient oriented in the $x$ axis
$cc_l$	=	sectional chord length times sectional coefficient of lift (ft)
$c_l$	=	sectional coefficient of lift
$C_L$	=	coefficient of lift
$c_m$	=	sectional pitching moment coefficient
$C_p$	=	coefficient of pressure
$N$	=	N factor
$r_{LE}$	=	leading-edge radius (nondimensionalized by local chord)
$Re_c$	=	Reynolds number (based on the sectional chord length)
$Re_\theta$	=	Reynolds number based on the attachment-line boundary-layer momentum thickness
$s$	=	arc length (nondimensionalized by local chord)
$t/c$	=	nondimensional thickness-to-chord ratio
$x$	=	Cartesian coordinate aligned down the body centerline
$x_r$	=	$x$ -location at which pressure recovery begins, nondimensionalized by local chord
$x/c$	=	$x$ -location nondimensionalized by local chord
$y$	=	Cartesian coordinate pointed out the starboard side of the vehicle
$y/c$	=	$y$ -location nondimensionalized by local chord
$z$	=	Cartesian coordinate pointed up from the ground (completes right hand rule)
$z/c$	=	$z$ -location nondimensionalized by local chord
$\alpha$	=	angle of attack, wind axis coordinate system (deg)
$\beta$	=	sideslip angle, wind axis coordinate system (deg)
$\Delta$	=	a difference
$\eta$	=	semispan location nondimensionalized by semispan length
$\theta$	=	sectional twist angle (deg)
$\Lambda_{LE}$	=	leading-edge sweep (deg)
$\phi$	=	an angle (deg)

\*Aerodynamics Research Engineer, Configuration Aerodynamics Branch, AIAA Senior Member.

†Senior Aerodynamics Research Engineer, Configuration Aerodynamics Branch, AIAA Associate Fellow.

‡Aerodynamics Research Engineer, Configuration Aerodynamics Branch, AIAA Member.

## Acronyms

<i>BLSTA3D</i>	=	Boundary Layer code for Stability Analysis
<i>CATNLF</i>	=	Crossflow Attenuated Natural Laminar Flow
<i>CDISC</i>	=	Constrained Direct Iterative Surface Curvature
<i>CF</i>	=	Crossflow
<i>HLFC</i>	=	Hybrid Laminar Flow Control
<i>LASTRAC</i>	=	Langley Stability and Transition Analysis Code
<i>LFC</i>	=	Laminar Flow Control
<i>NASA</i>	=	National Aeronautics and Space Administration
<i>NLF</i>	=	Natural Laminar Flow
<i>RANS</i>	=	Reynolds-averaged Navier-Stokes equations
<i>SUSAN</i>	=	SUBsonic Single Aft eNgin
<i>TS</i>	=	Tollmien–Schlichting
<i>USM3D-ME</i>	=	Unstructured Mesh Three Dimensional-Mixed Element

## Subscripts

<i>max</i>	=	a maximum value
------------	---	-----------------

## I. Introduction

With increasing awareness of the impact of the aviation industry upon the environment, significant efforts have been invested in new technology to reduce aircraft emissions. Research indicates that, in 2018, carbon dioxide emissions from aviation accounted for more than 2.5% of all global carbon dioxide emissions [1]. Consequently, the United Nations International Civil Aviation Organization has challenged the global aviation industry to achieve net-zero emissions by 2050. Technology improvements to reach these goals include, but are not limited to, advanced propulsion systems, cutting-edge materials coupled with novel manufacturing techniques, optimized city-pair mission profiles, and aerodynamic improvements. Improved aerodynamic performance can be realized through drag reduction, which may involve the use of laminar flow over some of the aircraft.

It is known that a laminar boundary layer causes decreased skin friction relative to a turbulent boundary layer, thus yielding drag savings. In addition to decreased viscous drag, laminar flow can also result in a reduction of profile drag, which yields additional efficiency improvements. Laminar flow can be achieved with active laminar flow control (LFC), hybrid laminar flow control (HLFC), passive flow control, or natural laminar flow (NLF). Relative to a flow-control method, the lack of control systems to implement NLF results in decreased system complexity, cost, and weight, all are desirable characteristics. Laminar flow is of interest to industry as production aircraft have been designed and delivered with laminar flow. NLF has been implemented on the HondaJet (NLF wing and fuselage nose), Boeing 787 (NLF nacelle), and Boeing 737 MAX (NLF winglet). An HLFC horizontal and vertical tail were implemented on the Boeing 787-9. The three NLF applications involve either low Reynolds number or low-sweep components. In general, NLF on the wing is a challenge due to rapid growth of crossflow instabilities, which grow quickly on components with an elevated Reynolds number and/or high sweep. Consequently, advanced design techniques are needed to control the crossflow growth for high-sweep and/or high-Reynolds-number components.

New design methods have been developed such that NLF can be sustained on transonic, swept-wing configurations. In particular, the Crossflow Attenuated Natural Laminar Flow (CATNLF) design method has been developed at the NASA Langley to achieve NLF on such components [2, 3]. This CATNLF method has been validated in the National Transonic Facility, and work is actively underway to support a transonic, high-Reynolds-number flight-test campaign [4–6]. This technique relies upon tailoring the suction surface pressure distribution of lifting components to control both crossflow and Tollmien–Schlichting instabilities that cause transition. In general, favorable pressure gradients, such as those near the leading edge of an airfoil or wing, promote crossflow growth while adverse pressure gradients result in increased Tollmien–Schlichting instabilities. Because instabilities can grow in both favorable and adverse pressure gradients, surface pressure distributions must be crafted to balance instability growth while still achieving desirable aerodynamic performance.

In general, the crossflow challenge exists on swept surfaces, which has resulted in the development of design efforts for wings. However, NLF is also of interest on other components, such as the vertical and horizontal tails. As previously mentioned, the Boeing 787-9 contains an HLFC system on both the horizontal and vertical tails, which

results in a reduction in drag [7]. Efforts in this paper are motivated by the desire to achieve tail drag reduction without a flow-control system. Relative to a wing, tails have unique challenges and benefits that must be considered. These challenges include low lift, a wide range of off-design certification requirements, and large control surfaces. Advantages of tails include the lack of leading-edge high-lift devices and minimal access panels. Even with some challenges, achieving drag reduction on the tails due to laminar flow is of interest.

The CATNLF design approach was originally developed for the NLF design of the suction surface on lifting components, for which the pressure surface shape is unconstrained to meet geometry constraints. For vertical tail design, NLF is desired on a nonlifting component, which has a symmetric airfoil geometry. In this case, a target pressure distribution must be achieved on both airfoil surfaces and geometry constraints cannot be directly enforced without over constraining the design. A novel CATNLF design approach was required for the NLF design of symmetric, nonlifting airfoils. A target pressure architecture was developed for symmetric NLF airfoils that implicitly satisfies geometry constraints while suppressing crossflow and Tollmien–Schlichting boundary layer instabilities.

This paper discusses the design of horizontal and vertical tails with the CATNLF technique. An overview of design and analysis tools is followed by a summary of the newly-developed design philosophy. Implementation of these new methods on a technology-development T-tail transport aircraft is then presented. A final section outlining conclusions and future work finishes the paper.

## II. Analysis and Design Approach

This technology-development study utilized a suite of computational tools including geometry and grid generation programs, a flow solver, a design code, and transition prediction software. All these tools supported the aforementioned CATNLF design method and will be herein discussed. A discussion of key characteristics and design criteria of the design method closes this section.

Geometry and grid generation were performed with a closely-coupled suite of tools from Helden Aerospace. Initial geometry preparation was performed with HeldenTool, a computer aided drawing tool that was used to prepare surfaces for subsequent grid generation [8]. A grid was then generated on the prepared geometry using HeldenMesh, a three-dimensional, mixed-element (prisms in the boundary layer), unstructured grid generator. The viscous region is generated with the advancing-layer method, and the outer volume is created with the advancing-front technique [9]. Computational analysis and design was then performed on this resulting volume grid.

A flowchart depicting the analysis and design process is shown in Fig. 1(a). These methods include the analysis/design loop on the right side of the schematic, as well as an external transition prediction loop shown on the left side of the image. The flowfield was computed with Unstructured Mesh Three Dimensional Mixed Element (USM3D-ME) flow solver [10, 11]. This cell-centered, finite-volume, unstructured, mixed-element solver was used with the Spalart-Allmaras (SA) turbulence model with rotation curvature correction and the 2000 model of the quadratic constitutive relation. The USM3D-ME flow solver was coupled with the aerodynamic design program, the Constrained Direct Iterative Surface Curvature (CDISC) code [3, 12]. CDISC is a knowledge-based design program in which a three-dimensional surface is determined from user-specified flow targets (e.g., sectional pressure distribution), integrated forces and moments, and geometric constraints. The design loop is repeated until the flow and geometry changes between successive design cycles are small and stable, typically requiring about 50 to 100 cycles. A companion paper at the 2024 SciTech Forum entitled “History and Status of the CDISC Aerodynamic Design Method” provides a detailed discussion of CDISC [12]. After convergence was achieved, the Boundary Layer Stability Three Dimensional (BLSTA3D) program was used to calculate both velocity and temperature profiles from the computed final pressures at each design station [13]. These data were subsequently analyzed with the Langley Stability and Transition Analysis Codes (LASTRAC) program, which was used to calculate the growth of Tollmien–Schlichting and crossflow instabilities [14]. Stability data were calculated with the linear stability theory  $e^N$  method including compressibility effects and no curvature effects. Transition was assumed to occur when either crossflow or Tollmien–Schlichting growth exceeded a user-prescribed critical  $N$  factor ( $N_{crit}$ ) of 9, which is representative of a cruise flight condition.

A CATNLF target pressure coefficient ( $C_p$ ) distribution is quite different than traditional turbulent  $C_p$  distribution, as seen in Fig. 1(b). As annotated, the CATNLF method relies upon rapid acceleration of the flow around the leading edge to mitigate the crossflow growth in this region. Due to the sweep angle and Reynolds number, crossflow growth occurs at the leading edge. However, the rapid acceleration controls the growth rate such that the associated  $N$  factors do not exceed the critical  $N$  factor. After this acceleration, a mild favorable pressure gradient exists up to the shock location, which is used to help control the crossflow and Tollmien–Schlichting growth. Contrary to a laminar design, a turbulent design may contain an adverse pressure gradient up to the shock such that the shock strength can be reduced.

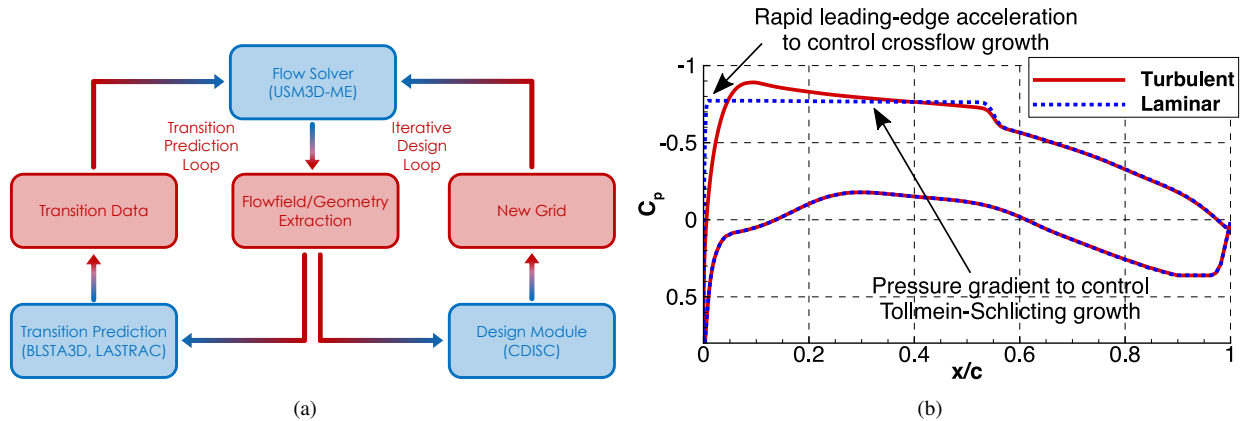


**Fig. 1** Depiction of CATNLF design method including (a) workflow and (b) resulting  $C_p$  distributions.

As a favorable gradient exists on a CATNLF-designed wing, the shock strength of a laminar wing is often greater than that of a comparable turbulent design. Despite the stronger shock relative to a turbulent wing, the viscous and profile drag savings for a laminar design are typically larger than the increased wave drag.

### III. Design Philosophy

As discussed in Sec. I, development of NLF on an aircraft empennage includes unique considerations relative to a wing. A typical wing has a stagnation point on the lower surface, seen as a red line in Fig. 2. Seen in green, a horizontal tail, which includes less lift than a wing, has decreased arc length from the attachment line (corresponding to the sectional stagnation point) to the leading edge of the airfoil section. While a typical horizontal tail produces negative lift, an inverted stagnation streamline is shown in the figure for ease of visualization. Shown as a blue line, the stagnation point on an ideal vertical tail is coincident with the leading edge, thus yielding no arc length between the stagnation point and leading edge. As the previously-developed CATNLF technique leverages the high curvature at the leading edge to accelerate the flow from the stagnation point to the upper surface, the CATNLF method in CDISC required some modifications to achieve NLF over a low-lift tail surfaces.

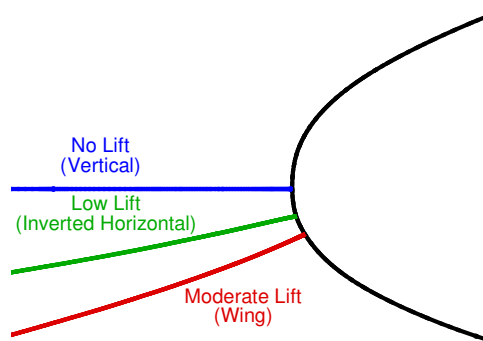


**Fig. 2** Stagnation streamlines for no-, low-, and moderate-lift airfoil sections.

In this section, the design approach to achieve NLF horizontal and vertical tails at flight Reynolds numbers and moderately-high sweep is presented. Material in the remainder of this section includes a discussion of the design challenges and also the novel design methods to achieve NLF on such surfaces. These methods are discussed first for a horizontal tail and second for a vertical tail.

### A. Horizontal Tail Design Philosophy

The design of a new horizontal tail must yield aerodynamic improvements relative to a baseline geometry while also satisfying a multitude of multidisciplinary design criteria. For instance, during transonic cruise, it is desirable for the horizontal tail to contain limited aft loading, especially over the elevator. This is desired for two main reasons. First, the aircraft maintains the stick-control feel for the pilot or control system such that the aircraft pitches up and down at approximately the same rate. Second, reduced loading on the elevator also results in smaller actuator size than for a heavily-loaded elevator near cruise. These design criteria were considered when developing the new NLF design methodology.

The CATNLF design methodology was applied to a horizontal tail, and key features are labeled in Fig. 3(a). Overall, the existing CATNLF design method could be implemented on a horizontal tail, but some of the constraints required special tailoring for this low-lift surface. Seen in the figure, three  $C_p$  curves are presented at a constant sectional lift coefficient for different laminar extents. A design parameter, denoted as  $x_r$ , is the  $x/c$  location for the end of the laminar run. This point nominally coincides with the point at which the pressure recovery begins. Aerodynamic efficiency is improved by ensuring the lower and upper surface  $C_p$  curves do not cross. The resulting reduction in lift in the downstream region counteracts the lift generated in the forward portion of the airfoil, which is not desirable. This adverse effect led to the modification of the basic target pressure generation constraint in CDISC such that the pressure curves do not cross. Returning to the figure, the pressure gradients over the airfoil were carefully crafted to control instability growth and promote laminar flow over much of the surface. With decreasing  $x_r$ , the amount of aft loading decreases and forward loading increases. Consequently, increased forward loading for  $x_r=0.50$  results in an adverse pressure gradient until  $x_r$  is reached. This adverse pressure gradient increases Tollmien–Schlichting faster for smaller  $x_r$  than larger  $x_r$ . Ultimately, the selection of  $x_r$  yielded transition points of 0.49, 0.55, and 0.65 for the three pressure distributions, thus confirming the effectiveness of using  $x_r$  as a design parameter.

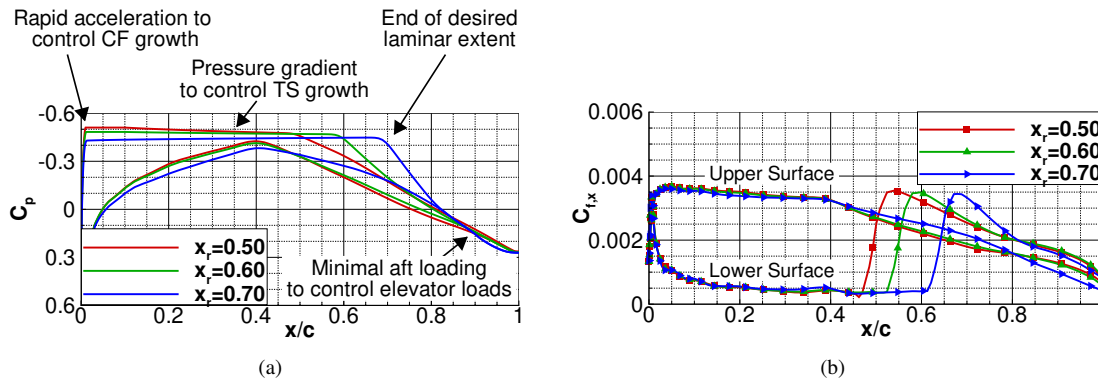


**Fig. 3 Effect of  $x_r$  on horizontal tail designs including (a)  $C_p$  and (b)  $C_{f,x}$ .**

Sectional cuts of skin friction in the streamwise direction ( $C_{f,x}$ ) is plotted for the three curves in Fig. 3(b). A reduction in  $C_{f,x}$  is realized over the laminar flow region of the lower surface relative to the upper surface for all three cases. After the transition point, where the skin friction returns to similar levels as turbulent flow, a gradual reduction in  $C_{f,x}$  is seen until the trailing edge, a trend that is readily seen for all three  $x_r$ . On the lower surface,  $C_{f,x}$  does not approach 0 at any points, which suggests adequate boundary-layer health. It is noted that small values of  $C_{f,x}$  are seen near the upper-surface trailing edge for  $x_r=0.70$ . This reduced  $C_{f,x}$  indicates the airfoil may be approaching separation on the upper surface. Based on these data, it was decided to use  $x_r=0.60$  for further design work as this maximizes the laminar run while protecting the section from trailing-edge separation.

Figure 4 shows the stability and transition results for the three  $x_r$  cases. The characteristic rapid leading-edge acceleration has yielded controlled growth of the crossflow  $N$  factor ( $N_{CF}$ ). For these cases,  $N_{CF}$  remains sufficiently below the critical  $N$  factor of 9. Further growth in crossflow aft of the leading edge is suppressed by a subsequent  $C_p$  gradient, evidenced by a reduction in crossflow downstream of the leading edge. Consistent with Fig. 3(a), the adverse pressure gradient associated with  $x_r=0.50$  yields faster Tollmien–Schlichting growth than the other two cases. It is observed that none of the  $N$  factors in Fig. 4 exceed  $N_{crit}=9$  across the analyzed range of  $x/c$ . Stability analysis was executed for the three cases up to the start of the pressure recovery region, where the adverse pressure gradient terminated the laminar boundary layer computation in BLSTA3D, presumably marking the transition point.

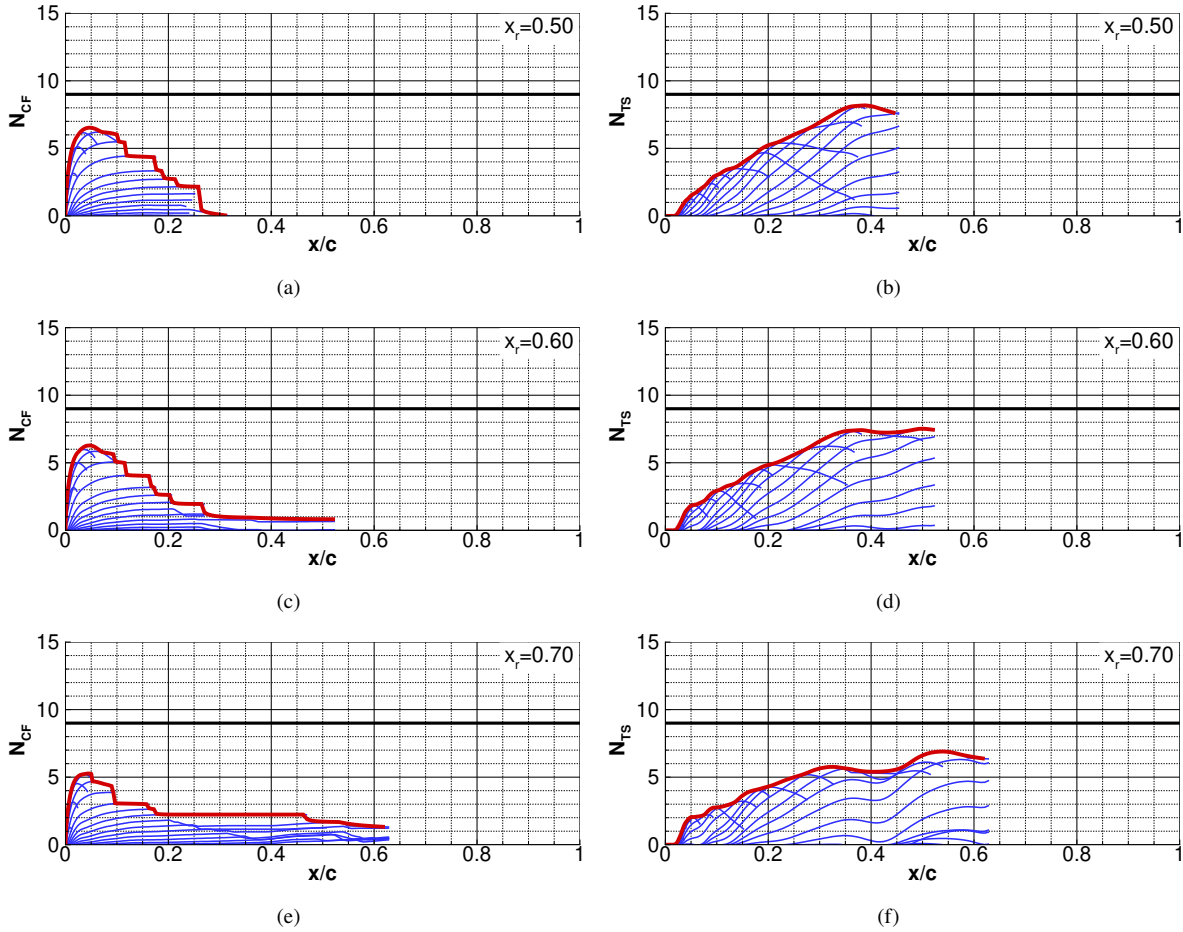


**Fig. 4** Stability and transition results including crossflow (left column) and Tollmien–Schlichting (right column) for three  $x_r$ .

## B. Vertical Tail Design Philosophy

While the horizontal tail generates limited lift, a vertical tail in an ideal midcruise condition generates no lift (side force). Consequently, the CATNLF method must be further extended to achieve NLF on such surfaces. The symmetric nonlifting airfoils used on the vertical tail have the attachment line at the leading edge and thus cannot take advantage of the flow around the leading edge to achieve the rapid acceleration needed for crossflow suppression. However, the crossflow peak level is affected by not only the rapid acceleration, but also the  $C_p$  value at the end of the acceleration, i.e., how long the boundary layer is exposed to the acceleration. Since the airfoil does not generate lift at cruise conditions with zero sideslip, it was proposed to try to stop the acceleration at decreased levels of  $C_p$  magnitude than the horizontal tail. Figure 5 shows computed and target pressures at the first and final design cycle. As shown in Fig. 5(a), the new target pressures (symbols) are the same as the initial analysis pressures (line) in the initial acceleration and pressure recovery regions. Significant differences are observed between  $x/c=0.005$  (selected to control the crossflow growth) and the minimum pressure location. In this favorable pressure gradient region, the target pressures are prescribed as a line connecting the pressures at these two end points. The points represent the desired chordwise location to end the rapid acceleration and approximately the location of the maximum airfoil thickness, respectively. As the design progresses and the analysis pressures shift toward the target pressures in the linear region, the geometry changes cause the pressure coefficients near the nose to show a more rapid acceleration ahead of  $x/c=0.005$ , with a subsequent flattening of the linear region ahead of the minimum pressure point. By the final design cycle shown in Fig. 5(b), the process has stabilized with a slight overshoot of the targets giving the desired rapid acceleration changing quickly to a nearly constant pressure region before growing linearly to the minimum pressure near midchord.

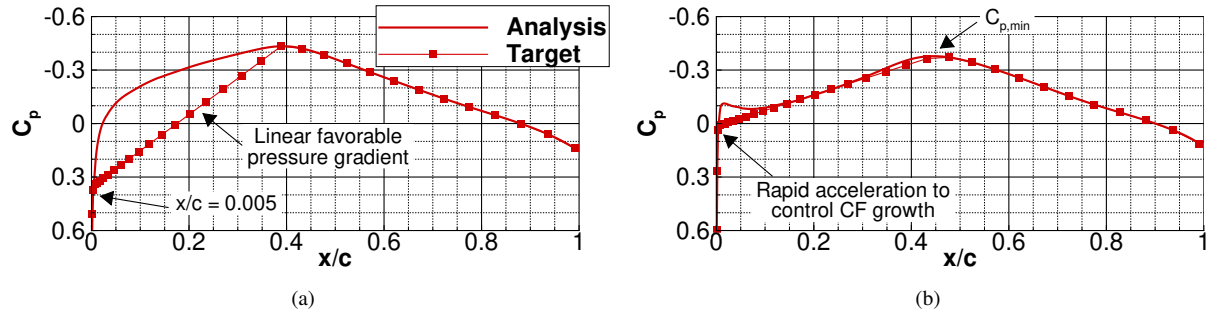


Fig. 5 Symmetric airfoil NLF target pressure development for (a) initial design cycle and (b) final design cycle.

An NLF airfoil was designed using this new CDISC constraint, and stability and transition data for this vertical tail section are shown in Fig. 6. A significant increase in  $N_{CF}$  is observed at the leading edge, which is subsequently suppressed by the sharp turn to a near-zero pressure gradient at  $x/c \approx 0.005$ . The subsequent favorable pressure gradient until  $C_{p,min}$  does cause significant regrowth of the crossflow instabilities in the midchord region, leading to transition at  $x/c = 0.37$ . No significant Tollmien–Schlichting growth is observed for  $x/c \gtrsim 0.1$ , which is immediately downstream of the  $C_p$  overshoot.

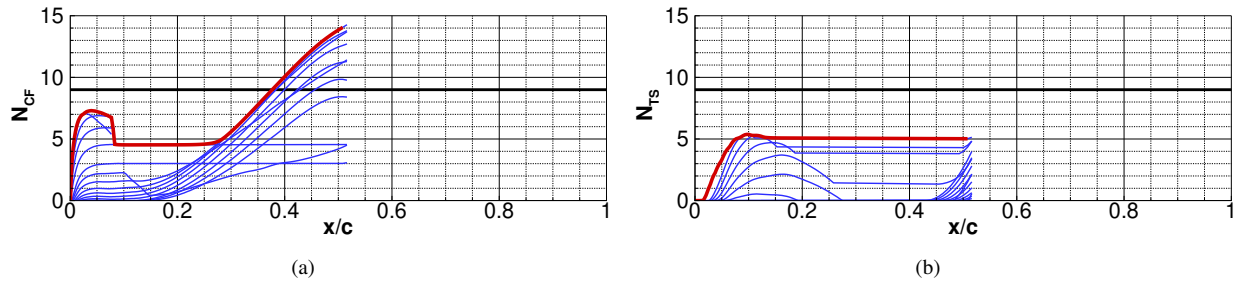


Fig. 6 Vertical tail stability and transition results including (a) crossflow and (b) Tollmien–Schlichting .

Figure 7 shows the airfoil that was developed to satisfy the design constraints. For this study, no specific requirement was defined for the maximum airfoil thickness, thus allowing the NLF design space to be freely explored. Early technology-development work was performed with airfoils as thin as  $t/c_{max} = 0.06$ . Because structural constraints require thicknesses larger than  $t/c_{max} = 0.06$ , the airfoil thickness was progressively increased to maximize laminar run and aerodynamic efficiency. As the crossflow growth is affected by the length of the acceleration region, decreased  $C_p$  at the end of the acceleration region will yield increased values of  $N_{CF}$ . With increasing thickness, the magnitude of  $C_{p,min}$  will increase, which subsequently causes increased crossflow growth. The airfoil shown in Fig. 7 corresponds to a maximum  $t/c$  of 0.095. A very-blunt leading-edge is observed in the geometry. Despite this blunt nature, the leading-edge radius is approximately 0.0052, which is a typical number for transonic airfoils [2]. Surface curvature of the airfoil ( $C$ ) near the leading edge of the airfoil is plotted in Fig. 7(b), as defined by

$$C = \frac{ds}{d\phi}. \quad (1)$$

In this equation,  $s$  is the nondimensional airfoil arc length and  $\phi$  is the angle relative to the  $x$  axis. As seen,  $C_{max}$  occurs slightly downstream of the leading edge, which is atypical of transonic airfoils in which  $C_{max}$  usually occurs at the leading edge.

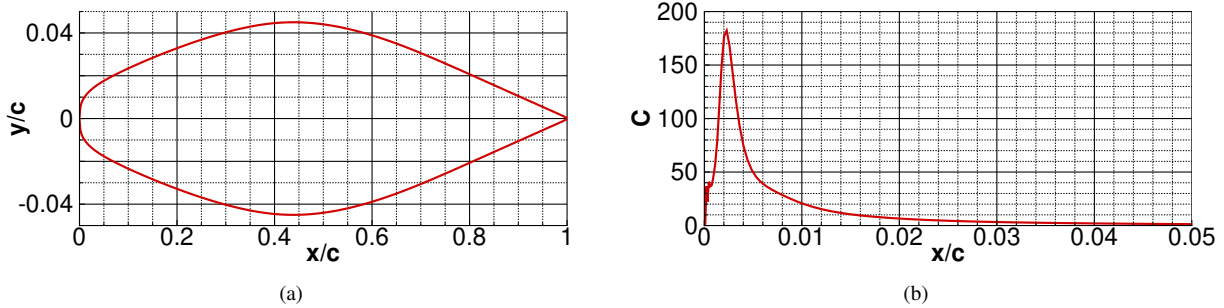


Fig. 7 Vertical tail airfoil section with (a) blown-up airfoil coordinates and (b) surface curvature.

#### IV. Empennage Design and Results

The developed design philosophy and tools discussed in Sec. III were applied to an aircraft configuration and subsequently analyzed at transonic conditions. Analysis of this geometry, at both midcruise and transonic off-design conditions, is discussed in this section.

##### A. Aircraft Configuration and Design Setup

While technology development can be applied to many different aircraft, the work in this paper was performed in direct support of the SUBsonic Single Aft eNginE (SUSAN) electrofan aircraft, as visualized in Fig. 8(a). This vehicle is a 180-passenger T-tail regional aircraft with a design range of 750 miles, maximum range of 2,500 miles, midcruise altitude of 37,000 ft, design  $C_L$  of 0.50, and a cruise Mach number of 0.785 [15]. It contains a distributed electric propulsion system and an aft-mounted turbofan engine. Empennage design and analysis in this project was performed on a simplified SUSAN configuration, seen in Fig. 8(b,c). As shown, no wing-mounted propulsion system was included to reduce computational complexity. This assumption is acceptable as the flow around the T-tail is minimally affected by such a propulsion system. A semispan aircraft was used for vehicle design and midcruise analysis. Off-design conditions with a nonzero sideslip angle were analyzed with a full-span aircraft.

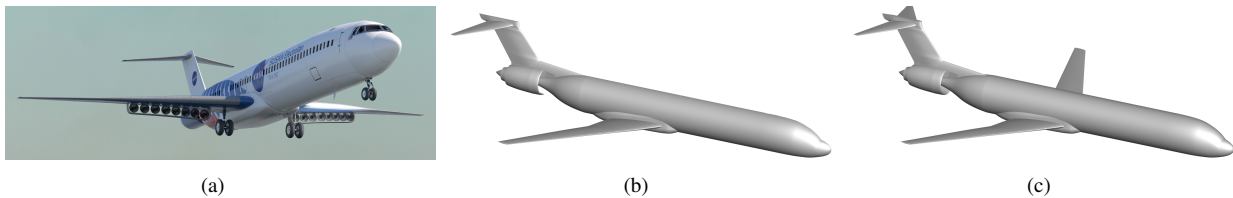
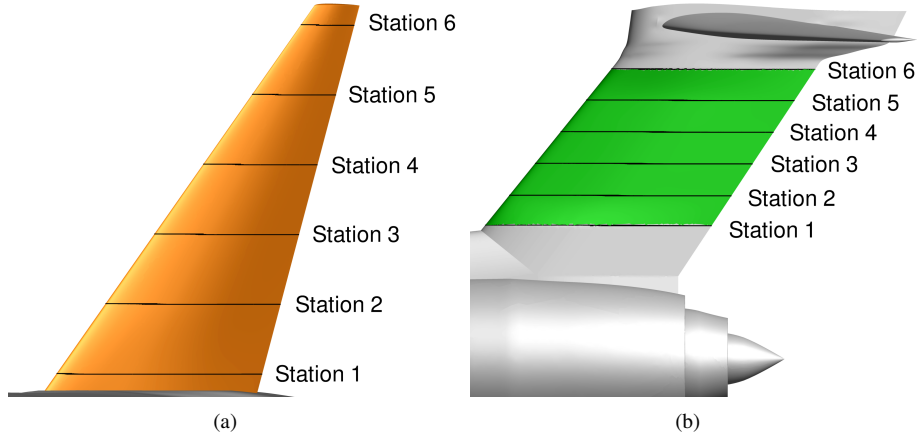


Fig. 8 SUSAN configuration including (a) graphical depiction, (b) semispan computational loft, and (c) full-span computational loft.

Figure 9 shows the regions of the tails that were designed. The black lines depict the six design stations on both tails. For the horizontal tail, the design was extrapolated from Station 1 to the root and Station 6 to the tip. The case of the vertical is slightly more nuanced. For this component, design was performed at Stations 2 through 5 with unchanged sectional geometry at Stations 1 and 6. Stations 1 and 6 on the vertical tail were held constant such that the NLF-designed region could smoothly integrate with the preexisting loft. Extrapolation was applied to transition from the design region to these outermost design stations. Table 1 presents physical characteristics of the tails including the leading-edge sweep and the  $Re_c$  based on the sectional chord length at the midcruise design point for all design stations.

##### B. Horizontal Tail Midcruise Performance

An NLF horizontal tail was designed using the methods and best practices as documented in Fig. 3. Implementation of these procedures and tools yielded the  $C_p$  curves plotted in Fig. 10, one at each design station. To aid in visualization



**Fig. 9** Design region and stations for (a) horizontal and (b) vertical tail surfaces.

**Table 1** Tail Characteristics at Midcruise Design Point.

	$\Lambda_{LE}$	$Re_c \times 10^6$ Station 1	$Re_c \times 10^6$ Station 2	$Re_c \times 10^6$ Station 3	$Re_c \times 10^6$ Station 4	$Re_c \times 10^6$ Station 5	$Re_c \times 10^6$ Station 6
Horizontal	35.0	16.3	13.9	11.5	9.07	6.66	4.25
Vertical	39.9	22.2	21.8	21.3	20.9	20.4	20.0

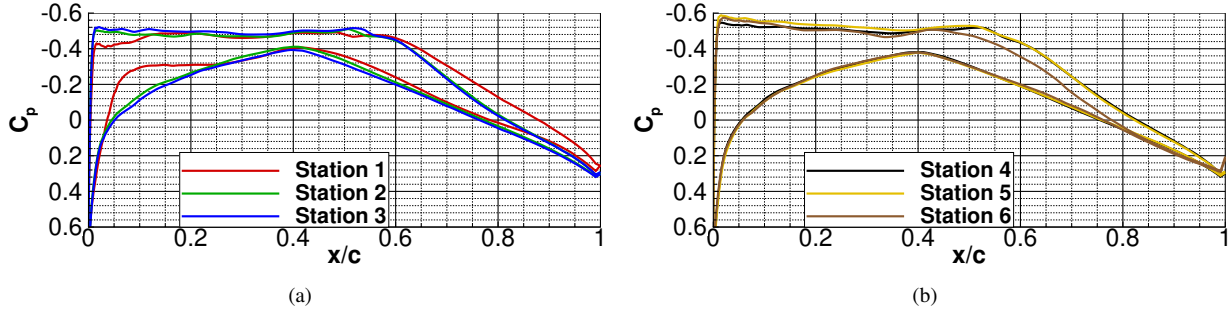


**Fig. 10** Horizontal tail pressure cuts promoting NLF at three (a) inboard and (b) outboard design stations.

and avoid excessive clutter, data are split between two different plots. In general, the previously-developed technology highlighted in Sec. III could be readily applied to all six design stations on the horizontal tail. Extremely similar  $C_p$  data are seen for the four middle design stations with slight deviations at the root and tip. Modifications to the Station 1  $C_p$  distribution were necessary due to close proximity of the vertical tail. At Station 6, tip effects resulted in some minor differences in the aft loading relative to the inboard stations. All stations exhibit the aggressive leading-edge pressure gradient to attenuate crossflow and a subsequent shallow pressure gradient to control Tollmien–Schlichting growth until nearly  $x_r$ , which was defined as 0.60. Downstream of  $x_r$ , pressure is recovered toward the freestream values.

Spanwise characteristics of the horizontal tail are shown in Fig. 11, which include sectional  $cc_l$  (in which  $c$  is the local chord length in feet and  $c_l$  is the sectional lift coefficient), sectional pitching moment ( $c_m$ ), leading-edge radius ( $r_{LE}$ ), and twist angle ( $\theta$ ) in degrees. For the given planform,  $c_l$  values were selected to achieve a desired spanwise lift distribution. This lift distribution [Fig. 11(a)] was selected such that the sectional  $cc_l$  would yield a nominally

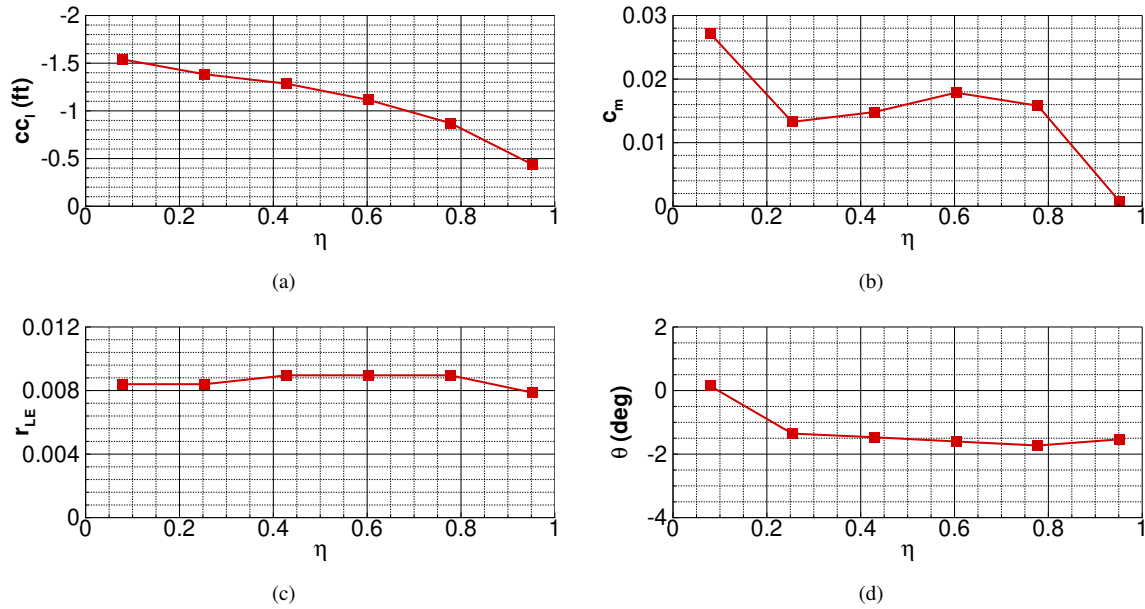


**Fig. 11 Spanwise data for horizontal tail including (a)  $c_{c_l}$  (ft), (b)  $c_m$ , (c) leading-edge radius, and (d) twist.**

elliptic load distribution to reduce drag. While an elliptic load distribution minimizes induced drag for subsonic and incompressible flow conditions, compressibility effects and wave drag generated at transonic conditions cause the minimum drag spanload to be different than an elliptic load distribution. However, as no strong shocks exist at any of the six stations on the tail, the effect of wave drag was deemed to be significantly less than that of induced drag, thus resulting in the desire for a nominally-elliptic load distribution. Sectional  $c_m$  data are shown in Fig. 11(b). The minimal aft loading on the sections results in decreased pitching moment magnitude relative to a traditional wing design, which can be in excess of 0.10 in magnitude [16]. The leading-edge radius, presented in Fig. 11(c), was free to change during the design process to help generate the desired pressure distribution. These small radii, all less than 0.01, are similar to radii previously seen on CATNLF-designed wings [16]. Figure 11(d) shows the spanwise twist distribution  $\theta$ . Some smoothing was applied during the design process to avoid abrupt changes in twist.

Both crossflow and Tollmien–Schlichting instabilities were calculated at all six design stations, and these data are shown in Fig. 12. As desired, the crossflow instabilities are attenuated at the leading edge with a maximum  $N$  factor of approximately 7.5 at Station 1. These crossflow instabilities at all stations are subsequently suppressed over the rooftop region during which the Tollmien–Schlichting instabilities grow. Progressive growth of  $N_{TS}$  over the rooftop is observed with transition occurring close to where pressure begins to be recovered. Decreased peak  $N_{CF}$  instabilities are observed at outboard stations, which contain a shorter chord and lower sectional Reynolds number, relative to the root.

Previous research has suggested that the Reynolds number based on the attachment line boundary layer momentum thickness ( $Re_\theta$ ) can be used to classify the state of a boundary layer at the attachment line [17, 18]. Attachment-line contamination occurs when the turbulent fuselage boundary layer impinges on a surface (e.g., vertical tail) and causes turbulent flow at the leading edge. In this case, a total loss of laminar flow may be realized. However, relaminarization of the fuselage turbulent boundary layer is possible if  $Re_\theta$  is less than 100. After relaminarization occurs, the desired laminar flow can be retained at outboard stations as long as  $Re_\theta < 235$  for each of these stations. These  $Re_\theta$  results are plotted in Fig. 13. Seen in the image, the inboard-most station yields an  $Re_\theta$  of approximately 100, the value needed to relaminarize the boundary layer. However, it is difficult to conclusively establish whether the flow sufficiently relaminarizes at this station or not. First, the value is very close to 100, which is not a definitive threshold. Second, the boundary layer impinging on the T-tail horizontal tail is significantly smaller than a fuselage boundary layer that intersects with a wing. It has been estimated that it is necessary to contain  $Re_\theta < 100$  for approximately 50 boundary layer heights to maintain laminar flow. Overall, the impact of this thin, turbulent boundary layer on the horizontal tail is not conclusively known. The laminar front, shown in Fig. 13, is plotted on the lower surface of the horizontal tail and is a pictorial representation of the previously-tabulated transition points.

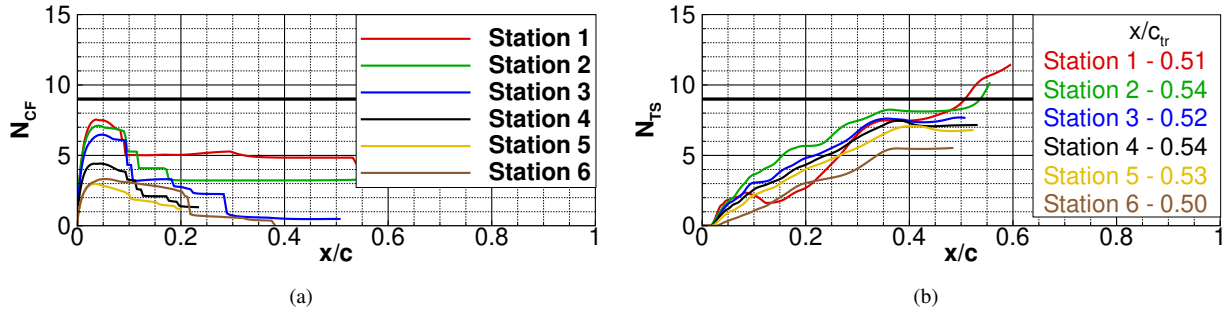


Fig. 12 Stability and transition data for designed horizontal tail at midcruise condition including (a)  $N_{CF}$  at all stations and (b)  $N_{TS}$  at all stations.

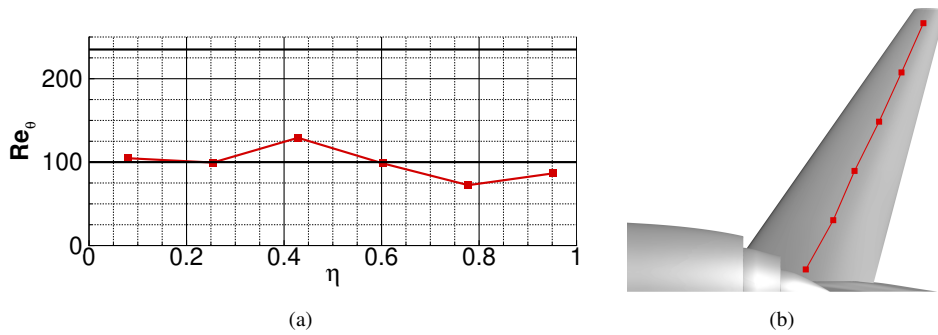


Fig. 13 Laminar flow horizontal tail (a) spanwise variation of  $Re_\theta$  and (b) laminar front.

### C. Vertical Tail Midcruise Performance

The aforementioned methods that were developed to yield NLF on a transonic vertical tail were applied to the SUSAN aircraft. Both  $C_p$  distributions and airfoil geometry cuts for the four design stations [see Fig. 9(b)] are plotted in Fig. 14. Consistent with Fig. 5(a), the rapid leading-edge acceleration is followed by a favorable pressure gradient until the minimum  $C_p$  point. The  $C_p$  distributions at all four stations are quite similar for  $x/c \lesssim 0.45$  with some differences observed throughout the pressure recovery. The four airfoil shapes that resulted in these  $C_p$  distributions are shown in Fig. 14(b) and are nearly coincident. Per the earlier discussion,  $t/c_{max}$  for the designed airfoils was selected to be 0.095. However, the baseline airfoils are defined by  $t/c_{max}=0.12$ , which required careful blending between the design regions and the rest of the vertical tail.

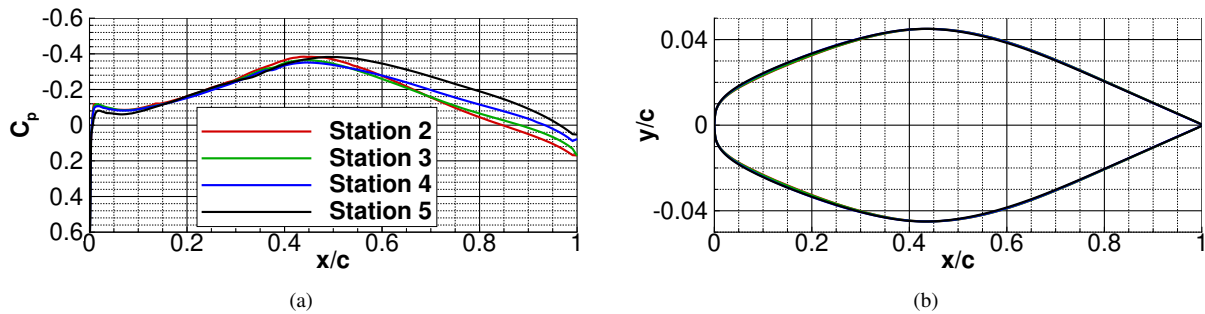
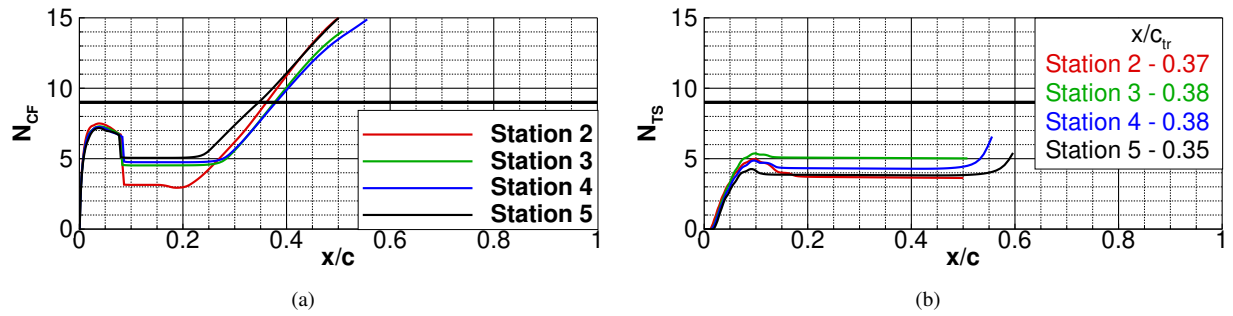


Fig. 14 Vertical tail cuts promoting NLF including (a)  $C_p$  and (b) airfoil geometry.

A composite of stability and transition data at the four design stations is plotted in Fig. 15. In these characteristic plots, it is seen that  $N_{CF}$  grows near the leading edge and then is immediately suppressed downstream of  $x/c \approx 0.02$ . The early crossflow attenuation is evident following the leading-edge flow acceleration, which coincides with an increase in Tollmien–Schlichting instabilities downstream of the acceleration but still in the forward portion of the airfoil. The maximum  $N_{CF}$  near the leading edge is approximately 7.1, which is sufficiently below  $N_{crit}$ . After this point, midchord crossflow regrowth and minimal Tollmien–Schlichting growth are observed. Transition is caused by the crossflow instabilities at all stations as  $N_{TS}$  is sufficiently below  $N_{crit}$  at all four of the designed stations. The pressure gradient was carefully crafted to balance both the crossflow and Tollmien–Schlichting instabilities.



**Fig. 15** Stability and transition data for vertical tail design stations at midcruise condition including (a)  $N_{CF}$  and (b)  $N_{TS}$ .

Results in Fig. 16(a) show  $Re_\theta$  as a function of nondimensional span station  $\eta$ . As seen, the inboard-most stations are close to 100, which may promote relaminarization of the boundary layer. In addition to satisfying  $Re_\theta < 100$ , attachment line protection could be realized through a device that diverts the turbulent flow away from the tail leading edge. A detailed examination of such behavior and applicability of  $Re_\theta < 100$  to vertical tails is warranted. Figure 16(b) shows the laminar front for the tail for the previously-tabulated values. The turbulent flow at Stations 1 and 6 is evident with laminar extent at the four interior design stations.

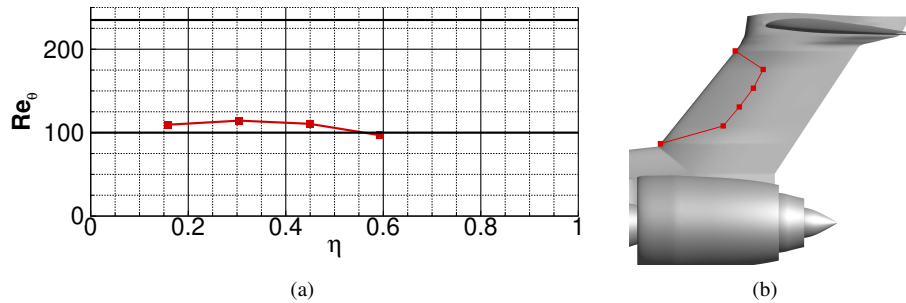


**Fig. 16** Laminar flow vertical tail inner four design stations (a) spanwise variation of  $Re_\theta$  and (b) laminar front.

It is difficult to quantify drag savings for the laminar design due to the absence of a well-designed baseline turbulent empennage. Consequently, the best metric was deemed to be the drag difference for the designed tails with and without laminar flow. Such comparisons must be performed at the same  $C_L$  between the two simulations, taken at the design point to be 0.50. In addition to the full aircraft, the component lift from the horizontal tail must also be matched for the two simulations, found to be  $C_{L,HT} = -0.0248$  at midcruise. In this case, a laminar flow on/off drag benefit of 3.0 and 1.4 counts was realized for the horizontal and vertical tails, respectively. The drag savings on the horizontal is greater than the vertical for two reasons. First, the laminar flow wetted area is larger on the horizontal. In addition, the horizontal tail has higher velocity flow over the lower surface than that seen on the vertical tail. This higher velocity flow produces increased skin friction levels, creating a greater potential for drag reduction when laminar flow is present.

## D. Off-Design Longitudinal Performance

While aerodynamic performance at the midcruise design condition is of great interest, the performance of the tails must be ensured in off-design conditions. Such analysis for a tail is quite complex as the effectiveness of the empennage must be ensured at a wide range of Mach number ( $M$ ), angle of attack ( $\alpha$ ), sideslip angle ( $\beta$ ), and control-surface deflection angles. This subsection investigates off-design performance at near-cruise transonic conditions.

### 1. Lift Effect

The midcruise condition for  $M=0.785$ ,  $C_L=0.50$ , and  $h=37,000$  ft with the baseline tail deflection angle results in  $\alpha$  of 2.27 deg. An angle-of-attack sweep centered around this angle was performed, resulting in  $C_L$  values of 0.32 through 0.67. Laminar fronts for seven of these simulations are plotted in Fig. 17. In general, a loss of laminar flow on the horizontal tail is observed with decreasing  $\alpha$ . Due to the downward-pointing lift vector on a horizontal tail, a decrease in  $\alpha$  results in increased loading on the horizontal tail. Increased flow acceleration results in earlier transition, caused by excessive Tollmien–Schlichting growth, for decreased  $\alpha$  cases relative to higher-lift cases. No significant changes are observed in the vertical tail laminar region.

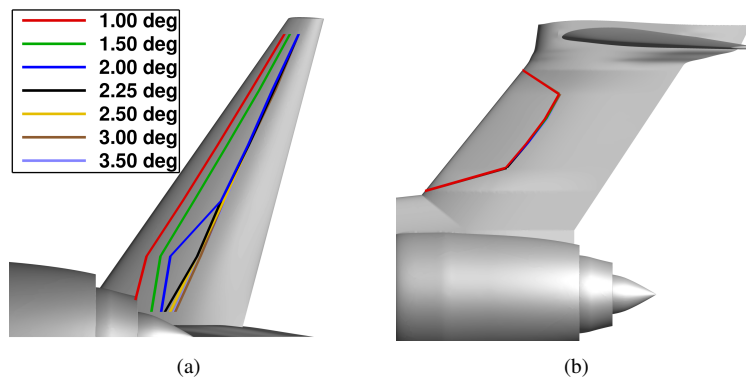


**Fig. 17** Effect of  $\alpha$  on laminar front for (a) horizontal and (b) vertical tails.

### 2. Mach Effect

In addition to deviations in  $C_L$ , it is desired for the vehicle to perform well across a range of Mach numbers. Data presented in Fig. 18 were calculated with a fixed tail incidence angle at  $C_L=0.50$  for  $0.70 \leq M \leq 0.86$  in which laminar fronts are shown on both tail surfaces. Overall, minimal effect on the laminar front is observed, which is encouraging. At the inboard stations on the horizontal tail, an increase in  $M$  results in a reduction of the laminar extent, seen as an upstream movement of the front. However, insignificant differences are observed outboard on the horizontal tail and vertical tail. The lack of a shock on the vertical tail, even at Mach 0.85, yields less impact due to Mach number variations on the laminar extent than for a traditional transonic design.

## E. Off-Design Lateral Performance

During transonic cruise, the aircraft is subjected to nonzero sideslip angles. In general,  $\beta$  is between 0 and 1.0 deg during steady, level transonic flight, and the associated data are shown in Fig. 19. Consequently, analysis of a full-span aircraft was performed at 0, 0.5, and 1.0 deg for  $\alpha=2.27$  deg, which yields the midcruise target of  $C_L=0.50$ . Pressure cuts on the windward and leeward surfaces of the horizontal tail for these three angles are shown in Fig. 19. The leeward surface is shown in the left column of plots, and the windward surface is the right column. Each row of plots corresponds to a given design station. For both the windward and leeward sides, Station 1 is defined to be closest to the aircraft centerline and Station 6 is the furthest outboard station. When considering the leeward  $C_p$  distributions [Fig 19(a,c,e)], the largest  $C_p$  differences due to  $\beta$  are observed at Station 1. With increasing  $\beta$ , the vertical tail generates increased side force, which will result in more aerodynamic interference to the horizontal tail than the no-sideslip condition. Stations 1 and 2 of the horizontal tail depict the effect of the lifting vertical tail on the horizontal tail. Increased acceleration (corresponding to a peak in  $C_p$ ) around the leading edge is observed for larger values of  $\beta$ . The effect of  $\beta$  decreases at

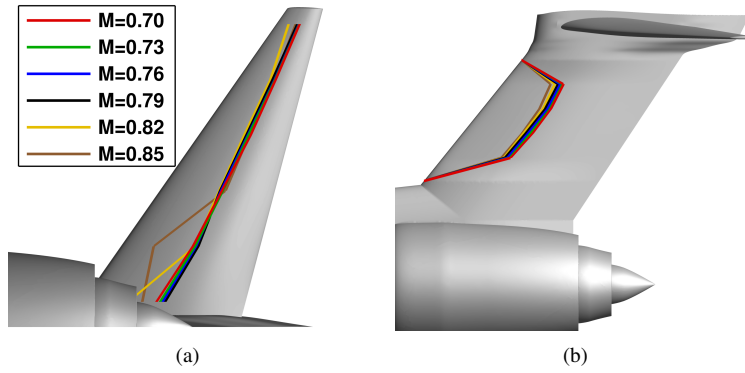


Fig. 18 Effect of  $M$  on laminar front for (a) horizontal and (b) vertical tails.

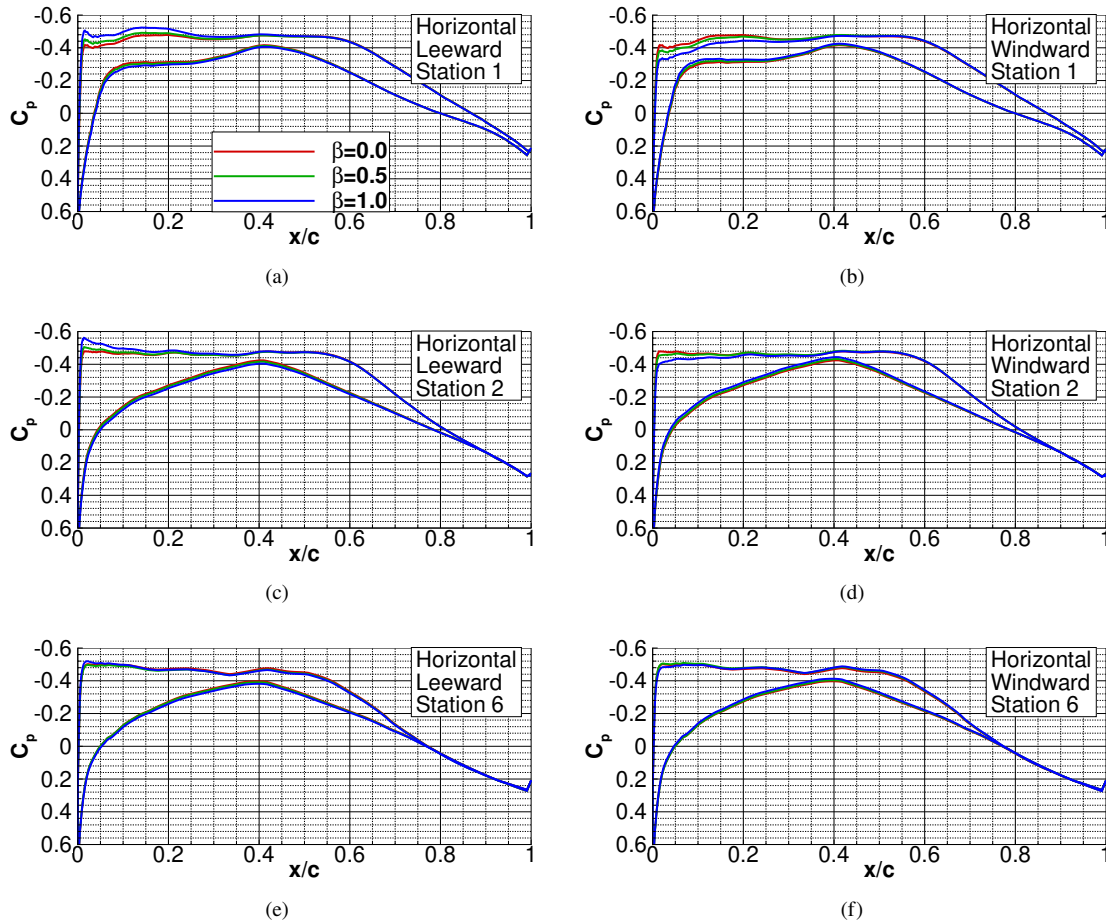
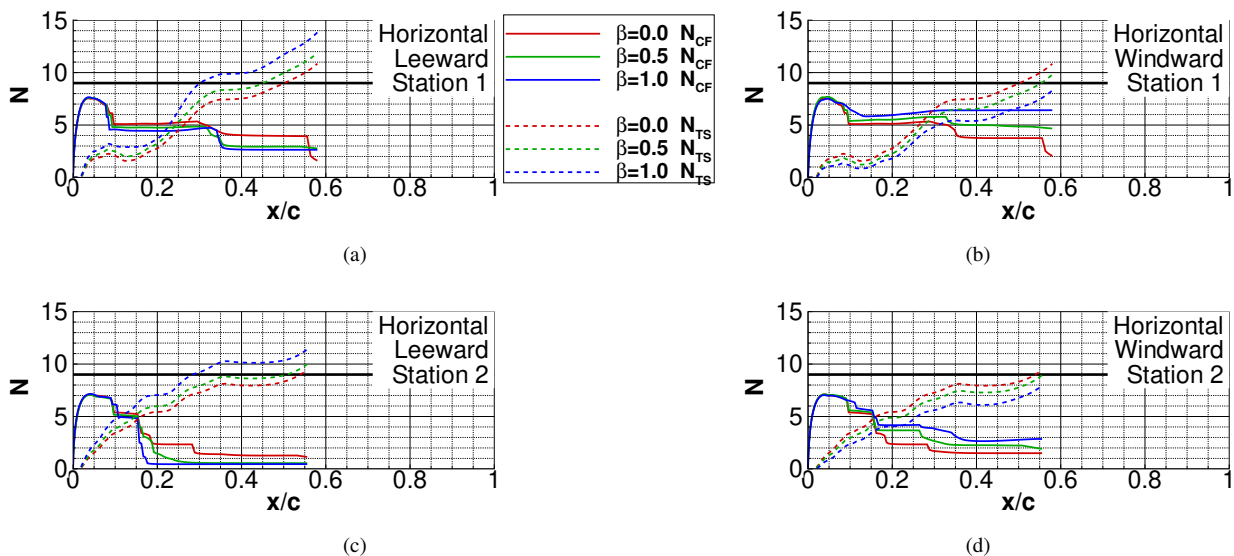


Fig. 19 Surface pressure cuts on leeward and windward horizontal tail surfaces at three design stations.

outboard span stations as the effect of the vertical tail is less pronounced at these stations. Inconsequential differences are observed for Station 6. For simplicity and brevity, Stations 3 through 5 are not presented as  $C_p$  trends are very similar to Station 6 in which no significant differences were observed.

Windward data on the horizontal tail are shown in the right column of plots, or Fig. 19(b,d,f). Similar to the leeward surface, the largest deviations in  $C_p$  are seen at the inboard stations with decreasing spread toward the tip. With increasing  $\beta$ , the stagnation point on the vertical tail shifts from the leading edge to the windward surface (not shown). The flow on the windward surface experiences less leading-edge acceleration, which in turn decreases the acceleration over the horizontal tail. This trend is particularly pronounced at Station 1 in Fig. 19(b). As the leading-edge acceleration is key to controlling the crossflow instabilities, reduced acceleration may inhibit laminar flow at these design stations.

Both crossflow and Tollmien–Schlichting instabilities are plotted in Fig. 20 on the windward and leeward surfaces at Stations 1 and 2. As the crossflow growth is particularly sensitive to the leading-edge acceleration and the resulting  $C_p$  peak, the similar behavior of crossflow near the leading edge of the section brings confidence to the methods used to attenuate the crossflow growth. While the crossflow data are nearly the same for all simulations, some differences are observed with the Tollmien–Schlichting instabilities. Notably, increased  $\beta$  results in increased Tollmien–Schlichting growth on the leeward surface and decreased Tollmien–Schlichting instabilities on the windward surface. The increased windward Tollmien–Schlichting growth is attributed to the differences in the leading-edge pressure gradient shown in Fig. 19. Overall, similar trends are observed in the instability behavior between the different sideslip angles and windward/leeward side of the vehicle, and this observation indicates that the laminar extent on the horizontal tail is dependent upon  $\beta$  near transonic cruise. Stations 3 through 6 are omitted as results are very similar to the two presented stations.



**Fig. 20** Crossflow and Tollmien–Schlichting instabilities on leeward and windward horizontal tail surfaces for Stations 1 and 2.

Laminar fronts on the leeward and windward horizontal tail surfaces for all three  $\beta$  values are plotted in Fig. 21. As previously discussed, decreased laminar flow is realized on the inboard portion of the leeward surface at  $\beta=1.0$  deg relative to the other cases. As the flow over the vertical tail accelerates, a decrease in laminar run on the horizontal tail is expected due to excessive Tollmien–Schlichting growth [Fig. 20(a,b)]. The effect of the vertical tail on the horizontal tail is less pronounced at outboard stations in which an inconsequential change in the laminar run is seen. Contrary to the leeward surface, minimal changes in laminar extent occur on the windward surface. It is evidenced that the change in  $C_p$  on the pressure (windward) surface of the vertical tail has minimal effect upon the horizontal, thus indicating that  $\beta$  has a significant effect upon the leeward laminar front relative to the windward surface.

Figure 22 shows vertical tail waterline cuts of  $C_p$  at Stations 2 and 5. Both windward and leeward pressures are shown for nonzero sideslip angles, and one curve is presented for the symmetric  $\beta=0$  condition. At the midcruise condition of  $\beta=0$ , the stagnation point of the flow is coincident with the leading edge of the vertical tail. With increasing  $\beta$ , the stagnation point progressively shifts onto the windward (pressure) surface. This behavior results in larger leading-edge acceleration onto the leeward surface and decreased acceleration for the windward surface. The differences

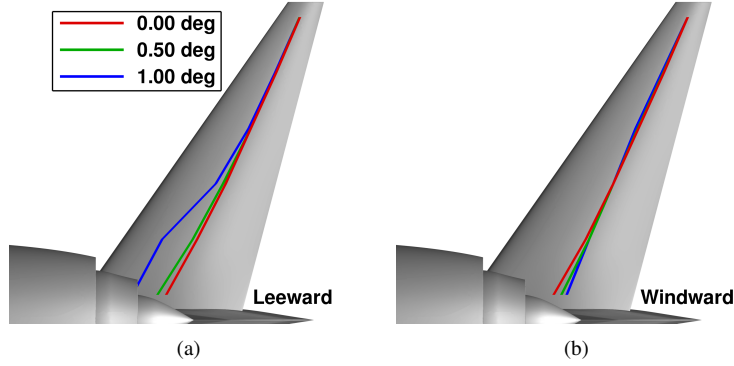


Fig. 21 Laminar flow for different crossflow angles on horizontal tail (a) leeward and (b) windward surfaces.

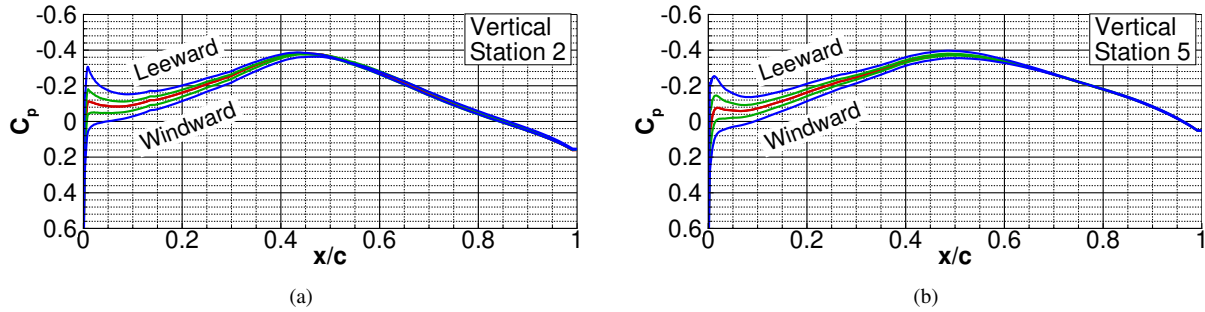
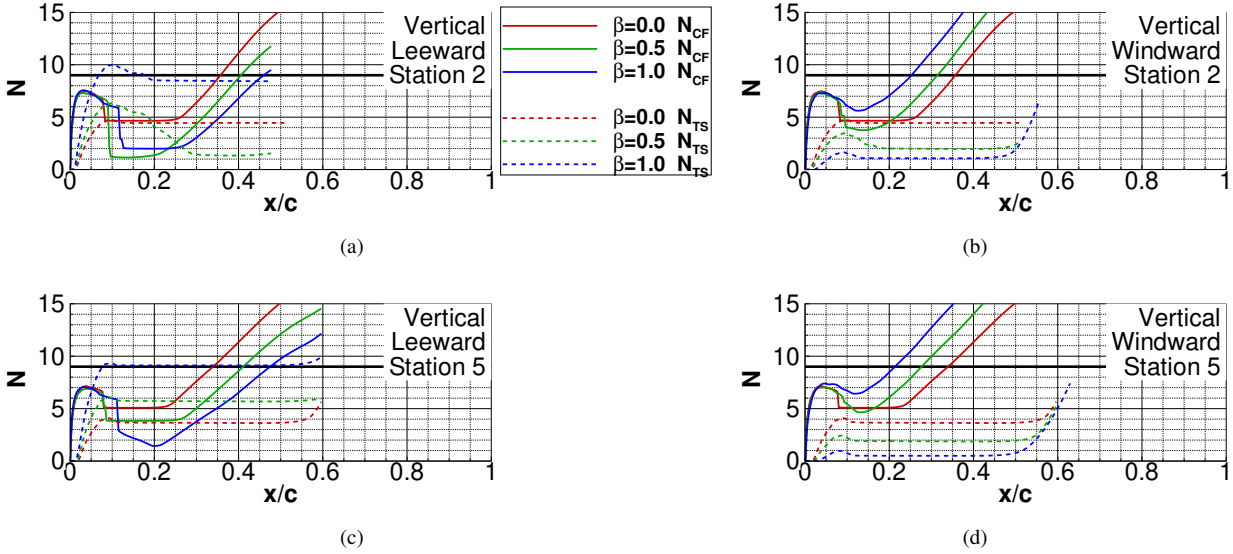


Fig. 22 Surface pressure cuts on vertical tail at (a) Station 2 and (b) Station 5.

are quite dramatic, and they affect the  $C_p$  distribution all the way until  $x/c \approx 0.6$ , well downstream of the predicted laminar run for  $\beta=0$  of  $x/c \approx 0.4$ . The pronounced differences in leading-edge  $C_p$  distribution is concerning as this adversely affects the instability results, plotted in Fig. 23. Pressure cuts at Stations 3 and 4 are not presented for brevity as the results are similar to those shown in the figure below.

The instability data for the windward and leeward side of the vertical tail at Stations 2 and 5 are presented in Fig. 23. Similar to the horizontal tail, large differences in the  $N$  factor behavior are observed for the three  $\beta$  simulations. There are differences in both crossflow and Tollmien–Schlichting growth amongst the simulations. As shown in Fig. 22, the leeward side of the vertical tail contains a sharp peak in  $C_p$  and a following favorable pressure gradient at the off-design sideslip angle cases analyzed. This behavior results in a significant decrease in laminar run, especially for  $\beta=1$  deg. While transition is caused by midchord crossflow regrowth for  $\beta=0$  deg, the large Tollmien–Schlichting growth downstream of the leading edge causes transition at  $\beta=1.0$  deg. On the windward surface, a stronger favorable pressure gradient is observed for larger sideslip angles, which causes increased midchord crossflow regrowth. Consequently, an upstream movement of the transition location is observed.

Figure 24 depicts the laminar extent for both surfaces of the vertical tail. Consistent with the previously-discussed instabilities, a marked reduction in laminar extent is seen on the leeward surface at  $\beta=1.0$  deg. This early transition is caused by excessive Tollmien–Schlichting growth immediately downstream of the leading-edge  $C_p$  peak (see pressures in Fig. 22). While a slight increase in laminar run is seen at 0.50 deg, a marked loss of laminar flow at  $\beta=1.0$  deg is observed. Consequently, to maintain laminar flow, the aircraft must operate at  $|\beta| \leq 0.50$  deg. Relative to the leeward surface, the windward surface indicates  $\beta$  has a decreased effect on laminar extent. The increased crossflow growth at larger sideslip angles results in decreased laminar extent for larger  $\beta$  relative to  $\beta=0$  deg.



**Fig. 23 Crossflow and Tollmien–Schlichting instabilities on leeward and windward vertical tail surfaces for Stations 2 and 5.**

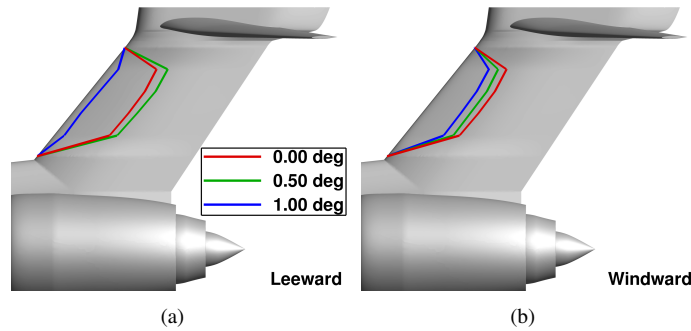


**Fig. 24 Laminar flow for different crossflow angles on vertical tail (a) leeward and (b) windward surfaces.**

## V. Conclusions

Design methods to promote natural laminar flow (NLF) at transonic conditions have been developed and subsequently applied to the SUBsonic Single Aft eNginE (SUSAN) T-tail aircraft. The previously-developed Crossflow Attenuated Natural Laminar Flow (CATNLF) design method was employed and extended to facilitate NLF on the empennage. The CATNLF method relies heavily upon rapid leading-edge acceleration to attenuate crossflow growth at the leading edge. This acceleration is caused by both careful tailoring of the geometry and leveraging additional acceleration of the flow from the stagnation point to the suction surface. Horizontal and vertical tails, which contribute low or no lift in midcruise conditions, do not generate the same leading-edge acceleration due to the stagnation point location. Consequently, novel techniques were developed to control both the crossflow and Tollmien–Schlichting growth without significant distance from the stagnation point to the leading edge. This paper presents the development of computational and design efforts to enable this technology.

A philosophical approach to develop empennage pressure distributions is presented. These efforts included leveraging the CATNLF design techniques as well as the development of new constraints for both the horizontal and vertical surfaces. Multidisciplinary design considerations require minimal loading over the aft portion of the horizontal tail, especially over the elevator. Consequently, the majority of the lift is carried by the forward part of an airfoil section. A

rooftop pressure gradient is sustained immediately downstream of the leading edge, and NLF is maintained in this region. Ultimately, methods were implemented to yield NLF on much of the surface, and best-practices were defined to seek NLF over 50-60% of the airfoil section, which resulted in a drag savings of about 3.0 counts at midcruise. The vertical tail, which generates no lift at the midcruise condition with  $\beta=0$  deg, required additional technology development. The resulting  $C_p$  distributions are markedly different than conventional transonic airfoils, whether turbulent or laminar. For this case, rapid leading-edge acceleration is followed by a gradual favorable pressure gradient. Midchord crossflow regrowth causes transition at approximately 40% of the chord. These new methods yielded drag savings of approximately 1.4 counts.

The high-fidelity design and computational analysis presented in this paper presents new design methods for empennage NLF and a transonic off-design analysis. Many design constraints and certification criteria must be satisfied for horizontal and vertical tails, both in the high- and low-speed flight regimes. This paper concerns cruise at transonic flight conditions. Future work should examine low-speed stability and control characteristics and ensure adequate performance and effectiveness of the surfaces outside of cruise. Additional considerations could be made for structural considerations, such as the maximum thickness required for sufficient structure. While designs in this paper were performed on a T-tail geometry, the performance of both the horizontal and vertical tails may be different for a conventional-tail configuration. The herein-developed design methods may need additional enhancements for such a configuration.

## VI. Acknowledgments

Appreciation is extended to Dr. Michael Bozeman of NASA Langley in the generation of a full-span aircraft grid. Funding for this project was provided through the SUSAN program, part of the NASA Convergent Aeronautics Solutions project. The efforts of Dr. Tim Chau at NASA Ames Research Center is appreciated for the configuration and CAD support. Many members of the the larger SUSAN team also contributed to this study including engineers and scientists at NASA Glenn Research Center, Ames Research Center, Langley Research Center, and Armstrong Flight Research Center.

## References

- [1] Lee, D., Fahey, D., Skowron, A., Allen, M., Burkhardt, U., Chen, Q., Doherty, S., Freeman, S., Forster, P., Fuglestedt, J., Gettelman, A., Leon, R. D., Lim, L., Lund, M., Millar, R., Owen, B., Penner, J., Pitari, G., Prather, M., Sausen, R., and Wilcox, L., "The Contribution of Global Aviation to Anthropogenic Climate Forcing for 2000 to 2018," *Atmospheric Environment*, Vol. 244, No. 117834, 2021, pp. 1–29.
- [2] Lynde, M. N., and Campbell, R. L., "Computational Design and Analysis of a Transonic Natural Laminar Flow Wing for a Wind Tunnel Model," AIAA Paper 2017-3058, AIAA AVIATION Forum, Denver, CO, 2017.
- [3] Campbell, R. L., and Lynde, M. N., "Building a Practical Natural Laminar Flow Design Capability," AIAA Paper 2017-3059, AIAA AVIATION Forum, Denver, CO, 2017.
- [4] Lynde, M. N., Campbell, R. L., Rivers, M. B., Viken, S. A., Chan, D. T., Watkins, A. N., and Goodliff, S. L., "Preliminary Results from an Experimental Assessment of a Natural Laminar Flow Design Method," AIAA Paper 2019-2298, AIAA SCITECH Forum, San Diego, CA, 2019.
- [5] Lynde, M. N., Campbell, R. L., and Viken, S. A., "Additional Findings from the Common Research Model Natural Laminar Flow Wind Tunnel Test," AIAA Paper 2018-3292, AIAA AVIATION Forum, Dallas, TX, 2019.
- [6] Lynde, M. N., Campbell, R. L., Hiller, B. R., and Owens, L. R., "Design of a Crossflow Attenuated Natural Laminar Flow Flight Test Article," AIAA Paper 2021-0173, AIAA SciTech Forum, Virtual, 2021.
- [7] Powell, A., and Vijgen, P., "Apparatus and Method for Passive Purging of Micro-Perforated Aerodynamic Surfaces," European Patent Office Filing Number EP2387529B1.
- [8] Hooker, R., and Wick, A., "HeldenMesh Suite Overview: New Capabilities & Future Development," Manual v. 4.15, August 7, 2023.
- [9] Pirzadeh, S., "Structured Background Grids for Generation of Unstructured Grids by Advancing Front Method," AIAA Paper 91-3223, AIAA Applied Aerodynamics Conference, Baltimore, MD, 1991.

- [10] Pandya, M. J., Jespersen, D. C., Diskin, B., Thomas, J. L., and Frink, N. T., “Verification and Scalability of Mixed-Element USM3D for Benchmark Three-Dimensional Flows,” *AIAA Journal*, Vol. 59, No. 11, 2021, pp. 4719–4738.
- [11] Pandya, M. J., Jespersen, D. C., Diskin, B., Thomas, J. L., and Frink, N. T., “Efficiency of Mixed-Element USM3D for Benchmark Three-Dimensional Flows,” *AIAA Journal*, Vol. 59, No. 8, 2021, pp. 2997–3011.
- [12] Campbell, R. L., Banchy, M. N., and Hiller, B. R., “History and Status of the CDISC Aerodynamic Design Method,” AIAA SciTech Forum, 2024.
- [13] Wie, Y.-S., “BLSTA: A Boundary Layer Code for Stability Analysis,” Tech. rep., NASA CR-19930005608, 1992.
- [14] Chang, C.-L., “The Langley Stability and Transition Analysis Codes (LASTRAC): LST, Linear & Nonlinear PSE for 2D, Axisymmetric, and Infinite Swept Wing Boundary Layers,” AIAA Paper 2003-974, AIAA Aerospace Sciences Meeting and Exhibit, Reno, NV, 2003.
- [15] Jansen, R. R., Kiris, C. C., Chau, T., Kenway, G. K. W., Machado, L. G., Duensing, J. C., Mirhashemi, A., Haglage, J. M., Timothy, Dever, P., Chapma, J. W., French, B. D., Goodnight, T. W., Miller, L. R., Litt, J. S., Denham, C. L., Lynde, M., Campbell, R., and Hiller, B., “Subsonic Single Aft Engine (SUSAN) Transport Aircraft Concept and Trade Space Exploration,” AIAA Paper 2022-2179, AIAA SCITECH Forum, San Diego, CA & Virtual, 2022.
- [16] Lynde, M. N., Campbell, R. L., and Hiller, B. R., “A Design Exploration of Natural Laminar Flow Applications for the SUSAN Electrofan Concept,” AIAA Paper 2022-2303, AIAA SciTech Forum, San Diego, CA & Virtual, 2022.
- [17] Poll, D., “Some Observations of the Transition Process on the Windward Face of a Long Yawed Cylinder,” *Journal of Fluid Mechanics*, Vol. 150, 1985, pp. 329–356.
- [18] Campbell, R. L., and Lynde, M. N., “Natural Laminar Flow Design for Wings with Moderate Sweep,” AIAA Paper 2016-4326, AIAA AVIATION Forum, Washington, D.C., 2016.